KeAi

CHINESE ROOTS
GLOBAL IMPACT

Contents lists available at ScienceDirect

Petroleum Science

journal homepage: www.keaipublishing.com/en/journals/petroleum-science



Original Paper

Adsorption of methane onto mudstones under supercritical conditions: Mechanisms, physical properties and thermodynamic parameters



Yang Wang $^{a, b}$, Hong-Fei Cheng $^{a, b, *}$, Qin-Hong Hu $^{c, **}$, Lang-Bo Jia d , Xi-Meng Wang e , Sha-Sha Gao $^{a, b}$, Luo-Fu Liu f

- ^a School of Earth Science and Resources, Chang'an University, Xi'an, Shaanxi, 710054, China
- b Key Laboratory of West Mineral Resources and Geological Engineering of Ministry of Education, Chang'an University, Xi'an, Shaanxi, 710054, China
- ^c Department of Earth and Environmental Sciences, The University of Texas at Arlington, Arlington, TX, 76019, USA
- d Exploration and Development Research Institute, Changaing Oil Field, PetroChina, Xi'an, Shaanxi, 710000, China
- ^e Department of Geology and Geophysics, Texas A&M University, College Station, TX, 77843, USA
- ^f State Key Laboratory of Petroleum Resources and Prospecting, China University of Petroleum (Beijing), Beijing, 102249, China

ARTICLE INFO

Article history: Received 23 March 2022 Received in revised form 16 May 2022 Accepted 16 August 2022 Available online 19 August 2022

Edited by Teng Zhu and Jie Hao

Keywords:
Supercritical methane adsorption
Excess adsorption
Adsorbed-phase density
Adsorption model
Thermodynamic feature

ABSTRACT

Since the mechanisms of methane-mudstone interactions are important for estimating shale gas reserves, methane adsorption under supercritical conditions of 30 MPa pressure and 303.15, 333.15, 363.15 K temperatures was studied to measure the excess methane adsorption in two mudstone samples from Yanchang Formation, Ordos Basin. Excess adsorption features inflection points where the amount of adsorbed gas changes from increasing to decreasing concentrations. Three methods (fixed, slope, and freely fitted density) were applied to calculate the adsorbed-phase density ($\rho_{\rm ad}$), which was then used to fit the measured excess adsorption. Two criteria, the goodness-of-fit and whether the fitting can obtain reasonable absolute adsorption, were applied to determine the most accurate model. Results indicated that the supercritical Dubinin-Radushkevich (SDR) model with freely fitted $\rho_{\rm ad}$ was the most reasonable model. The volume of adsorbed methane at 363.15 K is close to the micropore (d < 2 nm) volume of the corresponding mudstone. Considering the actual geological conditions, the adsorbed gas should be predominantly stored in micropores. Thermodynamic parameters reveal that the methane adsorption on mudstone is a physisorption process that is jointly controlled by the heterogeneity of, and interaction forces between the methane molecule and, the rock surface.

© 2022 The Authors. Publishing services by Elsevier B.V. on behalf of KeAi Communications Co. Ltd. This is an open access article under the CC BY-NC-ND license (http://creativecommons.org/licenses/by-nc-nd/4.0/).

1. Introduction

Shale gas is gas that is derived from and stored in organic-rich mudstone/shales. It can be biogenic or thermogenic in origin, or a mixture of both, and is chemically the same as gases contained in other environments (Curtis, 2002; Luo et al., 2016a, 2016b; Zhao

et al., 2016). Mudstone/shale is the fine-grained sedimentary rock composed of organic matter and inorganic minerals (mainly quartz, carbonates, and clays), generally with the majority of particles <0.0625 mm in diameter (Strapoć et al., 2010; Luo et al., 2018, 2020, 2021; Huang et al., 2020a; Wang et al., 2020a; Kuang et al., 2022; Liu et al., 2020a, 2022b). Methane is generally the main component of shale gas, and it can occur as the adsorbed phase on organic matter and/or clay particles, as the free phase in intra-/inter-particle pores and/or fractures, and as the dissolved phase in residual liquid petroleum and/or other geological fluid (Curtis, 2002). Among these processes, adsorption is the main mechanism for shale gas occurrence. Generally, the proportion of adsorbed gas in the total gas content is 20%—85%, showing the significant difference among different gas-bearing formations (Curtis, 2002; Tian et al.,

^{*} Corresponding author. School of Earth Science and Resources, Chang'an University, Xi'an, Shaanxi, 710054, China.

^{**} Corresponding author. Department of Earth and Environmental Sciences, The University of Texas at Arlington, Arlington, 76019, USA.

E-mail addresses: wangyang911228@163.com, yang.wang@chd.edu.cn (Y. Wang), h.cheng@chd.edu.cn (H.-F. Cheng), maxhu@uta.edu (Q.-H. Hu), jlb_cq@ petrochina.com.cn (L-B. Jia), ximengwang@tamu.edu (X.-M. Wang), gs8636@chd. edu.cn (S.-S. Gao), liulf@cup.edu.cn (L-F. Liu).

2016; Chen et al., 2020; Liu et al., 2020a, 2020b). Consequently, defining mechanisms of methane adsorption on mudstone/shale is critical in determining the volumes of gas in place (*GIP*) in shale reservoirs.

Previous studies of methane adsorption onto mudstone/shale mainly focused on the excess adsorption test, adsorption correction, geological factors controlling gas occurrence, and in-situ adsorption capacity estimation (Guo et al., 2013; Hou et al., 2014; Rani et al., 2019; Wang et al., 2019a; Huang et al., 2021; Onawole et al., 2021). Laboratory analyses of methane adsorption are mainly performed by volumetric and gravimetric methods (Gasparik et al., 2014; Gao et al., 2020; Han et al. 2022a). However, the actual temperature and pressure of in-situ gas-bearing formation are generally much higher than the critical temperature (190.65 K) and pressure (4.64 MPa) of methane (Li et al., 2018a; Wang et al., 2019a), and the methane will be present as a supercritical state. Actually, only the excess adsorption amount can be measured by laboratory tests. The excess adsorption amounts correspond to the amount of adsorbed gas that exceeds the free gas density (Gensterblum et al., 2013; Tang et al., 2017). That is, the difference between the excess and absolute adsorption amounts is the amount of adsorbed gas with the same density as the free gas. When the pressure is low (<~10-15 MPa), the amount of adsorbed gas is limited and thus its volume is usually ignored. In this case, the absolute adsorption is considered to be equal to the excess adsorption. In previous studies on methane adsorption, pressures up to 10-15 MPa have usually been applied to directly determine the adsorption capacity (Rexer et al., 2013; Weishauptová et al., 2017: Huang et al., 2020b). However, when the pressure is gradually increased, the amount of adsorbed gas correspondingly gradually increases, so that its volume cannot be ignored. In this situation, the absolute adsorption cannot be directly measured, and it must be converted from the excess adsorption by using the appropriate adsorption model and adsorbed-phase density (ρ_{ad}) (Zhou et al., 2018; Wang et al., 2019a).

Various excess adsorption models applied with different adsorbed-phase densities can be applied to fit the experimental adsorption amounts and so determine the adsorption capacity of different systems (Tang et al., 2017; Li et al., 2018b; Yang and Liu, 2020). Gasparik et al. (2014) used the Langmuir model with freely fitted ρ_{ad} to evaluate the geological factors controlling on the gas adsorption capacity in Posidonia and Scandinavian Alum Shales. Tang et al. (2017) evaluated the fitting error of nine different adsorption models on the excess adsorption and suggested that the dual-site Langmuir model is superior to others from the goodnessof-fit interpretation of adsorption behavior and prediction of adsorption isotherms beyond test conditions. Song et al. (2018) introduced a combination model (L-SDR) of the Langmuir and the supercritical Dubinin-Radushkevich (SDR) model, and demonstrated that it can predict adsorption better than the individual Langmuir and SDR models. Zhou et al. (2018) showed that the Langmuir and SDR models cannot always obtain reasonable absolute adsorption isotherms when applying the fixed ρ_{ad} to fit the excess adsorption. Wang et al. (2019) compared the fitting performance of the Langmuir and SDR models with both fixed and freely fitted ρ_{ad} for Wufeng-Longmaxi Shales and suggested that the SDR model exhibits the least relative error. Overall, a comprehensive consideration of multiple factors to optimize the appropriate excess adsorption model and ρ_{ad} for specific methane-rock adsorption processes is critical to define the methane adsorption mechanism and better evaluate the adsorption capacity.

The mechanism of gas adsorption onto shales/mudstones has been well investigated by many scholars which mainly focused on the marine shale (Wang et al., 2021a; Kim and Devegowda, 2022; Liu et al. 2022a,b,c). However, there is a large number of continental

organic-rich shale/mudstone developed in China, represented by the Triassic Yanchang Formation in the Ordos Basin. Therefore, methane adsorption tests at a pressure of up to 30 MPa at temperatures of 303.15, 333.15, and 363.15 K were conducted on two Chang 7 mudstones from the Yanchang Formation, Ordos Basin in this study, to (1) optimize the excess adsorption model to better interpret the methane-mudstone adsorption behavior and their thermodynamic behavior; (2) ascertain the diameter range of pore network where adsorbed methane mainly stored in; and (3) define the adsorption mechanism of methane onto Yanchang mudstones.

2. Materials and methods

2.1. Sample collection

Two core samples were collected from the Upper Triassic Yanchang Formation, Ordos Basin, which is the second-largest sedimentary basin in China (Wang et al., 2017; Guo et al., 2020). These two samples, sedimented in the lacustrine environment, are grayblack mudstones with no obvious lamination and were taken from depths of 2037 m (6683.1 ft) and 2617 m (8585.9 ft) (subsurface). The basic sample information is listed in Table 1. Each sample was ground into grains (passing through 60–80 mesh) to conduct low-temperature CO₂ and Ar physisorption isotherms for pore structure quantification, and to conduct methane adsorption tests for gas adsorption mechanism determination.

2.2. Low-temperature gas physisorption

Using the QuadraSorb Station 3 apparatus from QuantaChrome, CO₂ and Ar physisorption measurements were conducted to quantify the structure properties of pores <2 nm and of 2-100 nm in diameter, respectively. Granular samples (60-80 mesh, ~5 g each) were firstly outgassed under vacuum at 383.15 K for about 12 h to remove volatile materials and adsorbed moisture (Wang et al., 2019b). The physisorption tests of CO₂ and Ar were conducted at 273.0 K and 87.4 K, respectively, with relative pressures [balance pressure (P)/saturation pressure (P₀)] are 0.004-0.029 and 0.003–0.998, respectively. Compared with N₂ adsorption at 77.3 K, Ar adsorption at 87.4 K can provide isotherms with a high pore size resolution (Wang et al., 2020b). Additionally, the commonly used Barrett-Joyner-Halenda (BJH) model has been shown to underestimate the pore characteristics for narrow mesopores with diameters less than 20 nm by as much as 20%-30% (Thommes et al., 2015; Psarras et al., 2017). Therefore, the density functional theory (DFT) model was utilized to interpret adsorption data and obtain the pore structure properties, including pore volume (PV), specific surface area (SSA), and pore size distribution (PSD) (Wang et al., 2021b, 2022; Han et al. 2022b).

2.3. High-pressure CH₄ adsorption

2.3.1. Adsorption measurement

A highly sensitive magnetic suspension balance (ISOSORP-HP II Static from Rubotherm with precision of 0.01 mg) was applied to obtain methane adsorption isotherms at the specific temperatures. Methane adsorption tests were conducted at temperatures of 303.15, 333.15, and 363.15 K (\pm 273.25 K) with pressures of up to 30 MPa, which is higher than the critical temperature and pressure of methane; therefore, adsorption was under supercritical conditions. The test procedure generally includes four steps. The first step is to conduct blank measurement (using He gas) at the target temperature and within a pressure range of 0–7 MPa to determine the mass and volume of sample container ($m_{\rm cont}$, $V_{\rm cont}$). The samples (60–80 mesh, ~5 g each) were then loaded into the container

 Table 1

 Basic geochemical and mineralogical information of samples.

Sample	Well	Depth, m	TOC, %	R ₀ , %	S ₁ , mg/g rock	S ₂ , mg/g rock	T_{\max} ,	HI, mg/g TOC	Mineral composition, %				
							°C		Quartz	Carbonates	Clays	Feldspar	Pyrite
Y-1	C96	2617	5.97	0.66	3.11	20.55	442	344	16.7	2.2	35.8	11.5	33.8
Y-2	X44	2037	4.22	0.55	1.17	15.81	446	375	38.6	2.1	52.3	1.8	5.2

TOC: total organic carbon; R_0 : vitrinite reflectance; S_1 : free hydrocarbon content; S_2 : remaining petroleum generation potential; T_{max} : temperature at peak pyrolysis yield; HI: hydrogen index, $HI = S_2/TOC$.

and vacuum dried (378.15 K, 12 h) to eliminate the adsorbed moisture and other volatile components. Subsequently, a buoyancy measurement was conducted to determine the mass and volume of the sample (m_{samp} , V_{samp}) via the same process as the first step. Finally, adsorption amounts were collected at 15 different pressure points between 0 and 30 MPa by using pure methane (99.99%) with equilibration time at each pressure point of at least 60 min.

The balance reading ($m_{\rm meas}$) equals the difference between the sample mass, sample container, adsorbed methane, and the buoyancy applied to the sample and sample container. Then, the mass of adsorbed methane ($m_{\rm ad}$) can be expressed as:

$$m_{\rm ad} = m_{\rm meas} - (m_{\rm samp} + m_{\rm cont}) + \rho_{\rm b} \cdot (V_{\rm samp} + V_{\rm cont})$$
 (1)

where ρ_b is density of free-phase methane at experimental conditions.

2.3.2. Gibbs excess adsorption

Previous studies on methane adsorption have shown that the measured methane adsorption uptake reaches a peak at a pressure of about 10-15 MPa (Wang et al., 2019a). This phenomenon is the Gibbs excess adsorption (Gensterblum et al., 2013; Weishauptová et al., 2017). The excess adsorption amount $(n_{\rm ex})$ equals the portion of absolute adsorption amount $(n_{\rm ab})$ that exceeds the bulk gas density:

$$n_{\rm ex} = n_{\rm ab} - V_{\rm ab} \cdot \rho_{\rm b} = n_{\rm ab} \cdot (1 - \rho_{\rm b}/\rho_{\rm ad}) \tag{2}$$

where V_{ab} is the volume of adsorbed methane.

An appropriate model based on Gibbs adsorption theory is needed to fit the excess adsorption isotherms and calculate the absolute adsorption content, which is critical to assess the in-situ adsorbed gas content. Various fitting models based on different adsorption assumptions, such as Langmuir, *SDR*, and their revised forms, have been applied to simulate the adsorption isotherms (Gasparik et al., 2014; Weishauptová et al., 2017).

Assuming that the adsorbent surface is homogeneous and gas is monomolecular-layer adsorbed on it, the Langmuir model can be expressed as (Thommes et al., 2015):

$$n_{\rm ab} = n_0 \cdot \frac{P}{P_{\rm L} + P} \tag{3}$$

where n_0 is the absolute adsorption capacity; P_L is the Langmuir pressure at half of the adsorption capacity.

However, mudstone is heterogeneous due to its complex composition and the wide range of pore size distributions (Guan et al., 2020; Wang et al., 2022). The SDR model, therefore, was also applied to illustrate the gas adsorption on the mudstone surface in this study. It is based on the micropore filling assumption, and can be shown as:

$$n_{\rm ab} = n_0 \cdot \exp\left\{-D \cdot \left[\ln\left(\frac{\rho_{\rm ad}}{\rho_{\rm b}}\right)\right]^2\right\} \tag{4}$$

where *D* is an interaction constant, $D=(RT/\beta E)^2$. *R* is the universal

gas constant; T is the temperature (K); β is the adsorbate affinity coefficient; E is the characteristic energy (Tang et al., 2017).

According to Eq. (2), the Langmuir- and SDR-based excess adsorption models can be shown as.

$$n_{\rm ex} = n_0 \cdot \frac{P}{P_{\rm L} + P} \cdot \left(1 - \frac{\rho_{\rm b}}{\rho_{\rm ad}}\right) \tag{5}$$

$$n_{\rm ex} = n_0 \cdot \exp\left\{-D \cdot \left[\ln\left(\frac{\rho_{\rm ad}}{\rho_{\rm b}}\right)\right]^2\right\} \cdot \left(1 - \frac{\rho_{\rm b}}{\rho_{\rm ad}}\right) \tag{6}$$

Additionally, it has been observed that gas adsorption and absorption will occur concurrently during methane sorption (Dang et al., 2020). To interpret this phenomenon and further improve the fitting performance of isotherms, the absorption modeled by the Henry component was added to the above excess adsorption equations (Tang et al., 2017), which could be named as Langmuirand *SDR*-Henry model, respectively,

$$n_{\rm ex} = n_0 \cdot \frac{P}{P_{\rm L} + P} \cdot \left(1 - \frac{\rho_{\rm b}}{\rho_{\rm ad}}\right) + k \cdot \rho_{\rm b} \cdot \left(1 - \frac{\rho_{\rm b}}{\rho_{\rm ad}}\right) \tag{7}$$

$$n_{\rm ex} = n_0 \cdot \exp\left\{-D \cdot \left[\ln\left(\frac{\rho_{\rm ad}}{\rho_{\rm b}}\right)\right]^2\right\} \cdot \left(1 - \frac{\rho_{\rm b}}{\rho_{\rm ad}}\right) + k \cdot \rho_{\rm b} \cdot \left(1 - \frac{\rho_{\rm b}}{\rho_{\rm ad}}\right)$$
(8)

where k is an empirical parameter.

Unknown parameters in Eqs. (5)-(8) can be determined by fitting the experimental adsorption amount by a least squares minimization, with the fitting coefficient (R^2) generally higher than 0.99 (Wang et al., 2019a).

2.3.3. Methods for determining the density of adsorbed methane (ρ_{ad})

In order to calculate absolute adsorption, the ρ_{ad} must be determined. However, the ρ_{ad} cannot be directly measured via existing techniques. Consequently, three indirect methods were utilized to obtain the ρ_{ad} in this study. In Method I the ρ_{ad} assigned a fixed value of 0.424 g/cm³ (the liquid methane density) or 0.373 g/ cm³ (the van der Waals density) (Wang et al., 2019a). Method II is based on an extrapolation of falling segment of the excess adsorption isotherm, with excess adsorption amount as the y-axis and density of free methane as the x-axis. The excess adsorption will decrease with the increasing ρ_b after the pressure reaches a certain value. Consequently, the extrapolation line will intersect with the x-axis where ρ_{ad} equals ρ_{b} (Zhou et al., 2018). Method III is based on the free fitting of experimental adsorption amount by assuming ρ_{ad} as an unknown parameter (Wang et al., 2019a). The ρ_{ad} values obtained by the above three methods are referred to as fixed density, slope density, and freely fitted density, respectively.

2.3.4. Fitting error analyses

The Akaike's Information Criterion (AIC) was applied to assess the results of different excess adsorption models in fitting the

adsorption data and optimizing a model that best interprets data while containing the fewest freely fitted parameters. The model with the smallest AIC generally exhibits the best goodness-of-fit. When the number of observations (n, 15 in this study) is low, the corrected AIC (AIC_c) can be expressed as (Sugiura, 1978):

$$AIC_{c} = AIC + \frac{2k(k+1)}{n-k-1} = 2k + n\ln\left(\frac{RSS}{n}\right) + \frac{2k(k+1)}{n-k-1}$$
 (9)

where k is the number of the freely fitted parameter; *RSS* is the residual sum of squares between the measured and fitted data.

2.4. Thermodynamic features of methane-mudstone adsorption

The thermodynamic parameters, including enthalpy change (ΔH) and entropy change (ΔS^0) , can express the pressure change with the temperature at a specific absolute adsorption amount (i), and can be obtained via the Clausius-Clapeyron formula,

$$\ln\left(\frac{P}{P^0}\right)_i = \frac{\Delta H}{RT} - \frac{\Delta S^0}{R} \tag{10}$$

Here, P^0 is atmospheric pressure, 0.1 MPa. By plotting the $\ln P$ versus 1/T, the ΔH and ΔS^0 can be obtained from the slope and intercept of the fitting line, respectively. The isosteric heat at a specific surface coverage $(q_{\rm st})$ reflects the interaction strength between adsorbate and adsorbent, which equals to ΔH but with a negative sign,

$$q_{\rm st} = -\Delta H \tag{11}$$

The $q_{\rm St}^0$ is the isosteric heat at zero surface coverage when the pressure approaches 0, which is commonly called the limiting isosteric heat of adsorption. Gas adsorption conforms to Henry's law under a low-pressure condition,

$$V_{ab} = K \cdot P \tag{12}$$

Here, K is Henry's law constant. $q_{\rm st}^0$ can be obtained from K based on the Vant-Hoff formula,

$$\ln K = \frac{q_{\text{st}}^0}{RT} + C \tag{13}$$

When the V_{ab} is small enough, a Virial expansion form of Eq. (12) can be written as (Yang et al., 2014),

$$\ln\frac{1}{K} = \ln\frac{P}{V_{ab}} = -a_0 - a_1 V_{ab} \approx -a_0 \tag{14}$$

Here, a_0 and a_1 are Virial coefficients. Then, the relationship between a_0 and K can be approximately expressed as:

$$K = \exp(a_0) \tag{15}$$

Therefore, it is essential to determine the valid pressure range that conforms to Henry's law. Generally, it should be confined to the range where $V_{\rm ab} \cdot (1-P/P_{\rm max})$ is positively correlated with $P/P_{\rm max}$ with a linear fitting coefficient (R^2) greater than 0.95 (Dang et al., 2020). Once the valid pressure range is determined, the value of a_0 and K can be derived from the intercept of the plot of $\ln(P/V_{\rm ab})$ vs. $V_{\rm ab}$ within the valid pressure range [Eq. (14)]. Then, the $q_{\rm st}^{\rm St}$ can be determined from the slope of the plot of $\ln K$ vs. 1/T based on Eq. (13).

3. Results and discussion

3.1. Pore structure

Combined CO2 and Ar physisorption tests were utilized to

characterize the microscopic pore structure (Fig. 1, Table 2). The *PSD* of the studied samples shows a multi-peak feature. The total *PVs* are 0.00757 and 0.01202 cm³/g, and total *SSAs* are 7.79 and 13.9 m²/g, for Samples Y-1 and Y-2, respectively. Specifically, the volumes of micro-, meso-, and macro-pores (d < 2, 2–50, and 50–100 nm, respectively) are 0.00273, 0.00262, and 0.00222 cm³/g, respectively, for Sample Y-1, which account for 36%, 35%, and 29% of the total *PV*. Similarly, the volumes of micro-, meso-, and macro-pore are 0.00445, 0.00513, and 0.00244 cm³/g, respectively, for Sample Y-2, which account for 37%, 43%, and 20% of the total *PV*.

3.2. Excess adsorption of methane

Fig. 2 depicts the excess adsorption amounts normalized to sample weight. It shows the Gibbs excess adsorption data, with distinct inflection points where the adsorbed amounts begin to decrease. The excess adsorption amount is temperature-dependent. In the low-pressure range (i.e., stage of increased adsorption amount), the adsorption amount and its increasing rate (an increase of adsorption amount within a unit pressure) with increasing pressure under low-temperature conditions are larger than that under relatively high temperatures. The maximum $n_{\rm ex}$ values are 1.73, 1.48, and 1.32 cm³/g for Sample Y-1, and are 1.69, 1.41, and 1.21 cm³/g for Sample Y-2, at temperatures of 303.15, 333.15, and 363.15 K, respectively. Consequently, the lower the temperature, the greater the maximum excess adsorption amount. The pressure at the maximum adsorption amount increases with increasing temperature.

Additionally, in the high-pressure range (i.e., stage of decreased adsorption amount), the decreasing rate of adsorption amount (a decrease of adsorption amount within a unit pressure) with increasing pressure under low-temperature conditions is larger than that under relatively high temperatures. Specifically, the decreasing rates of Sample Y-1 are 0.0228, 0.0169, and 0.0135 cm³/ g/MPa, and that of Sample Y-2 are 0.0325, 0.0268, 0.0165 cm³/g/ MPa, at temperatures of 303.15, 333.15, and 363.15 K, respectively. As a result, the temperature effect on adsorption amount at a relative high-pressure stage (>25 MPa) is insignificant, and isotherms at different temperatures intersect with each other in some cases. Finally, based on the extrapolation of excess adsorption amount, when pressure is high enough (>30 MPa), adsorption amount at lower temperature (e.g., 303.15 K) will less than that at higher temperature (e.g., 303.15 and 363.15 K). A similar phenomenon has also been indicated by Gensterblum et al. (2013) for

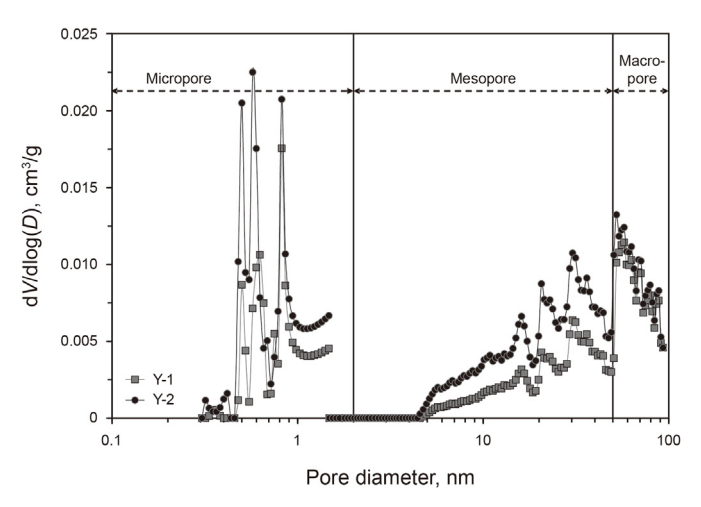
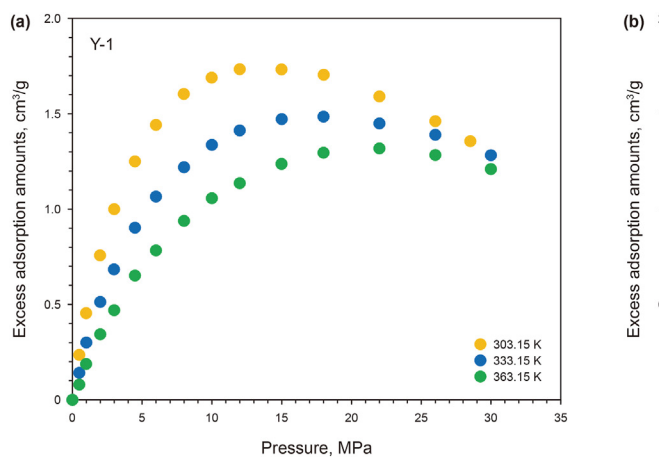


Fig. 1. Pore size distribution of studied samples.

Table 2Pore structure properties of studied mudstones.

Sample	Pore volume,	cm ³ /g		Specific surf	Specific surface area, m ² /g					
	micro-	meso-	macro-	total PV	micro-	meso-	macro-	total SSA		
Y-1	0.00273	0.00262	0.00222	0.00757	7.10	0.55	0.13	7.79		
Y-2	0.00445	0.00513	0.00244	0.01202	12.6	1.18	0.15	13.9		



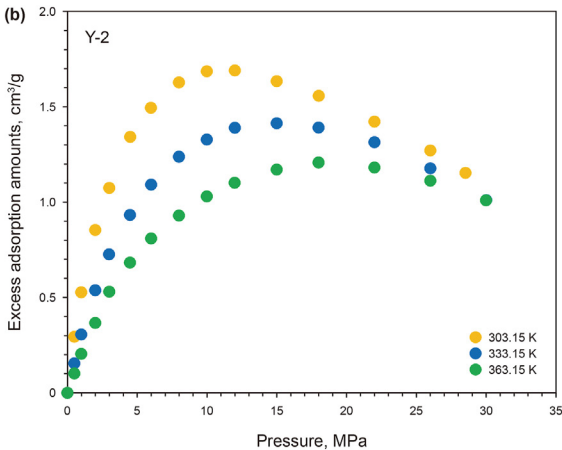


Fig. 2. Excess adsorption at different temperatures for (a) Y-1 and (b) Y-2.

three coal samples and Li et al. (2017) for Niutitang Shale from Southwest China.

3.3. Goodness-of-fit evaluation of various models

Two basic criteria need to be considered to evaluate the goodness-of-fit of various excess models of the adsorption data. Firstly, the fitting results should closely match the measured adsorption data with only a small deviation, which is the intuitive approach to initially decide whether the model can adequately describe the measured adsorption data or not. In addition, the absolute adsorption calculated from excess adsorption by the model correction should be reasonable and consistent with the adsorption theory.

3.3.1. Fitting performance and error

Fig. 3a-b show the fitted results of excess adsorption isotherms at 333.15 K by using the fixed density values (0.424 g/cm³ and 0.373 g/cm³) based on the Langmuir and SDR models. Results show a relatively good fit with adsorption amount for Sample Y-1, except for the SDR model with a density of 0.373 g/cm³. However, for Sample Y-2, results show a poor fit with adsorption amount in the high-pressure range. Wang et al. (2019a) also reported a poor fit when using adsorption models to simulate methane adsorption isotherms of Wufeng-Longmaxi Shales using the fixed ρ_{ad} . Zhou et al. (2018) reported that the absolute adsorption isotherms for the Longmaxi Shales decrease at high pressure when assuming an $\rho_{\rm ad}$ of either 0.424 or 0.373 g/cm³, which contradicts the adsorption theory that the absolute adsorption amount will reach a constant value as pressure increases. However, Chen et al. (2020) demonstrated that the fixed ρ_{ad} of 0.373 g/cm³ for adsorption correction is a convenient method to calculate absolute adsorption amounts of the Longmaxi Shale that are likely to be close to the actual value. In summary, evaluating whether the fixed density is applicable or not requires a study on the specific sample in question. In any event, it is no applicable to samples in this study.

The densities obtained via the slope intercepts in Method II are $0.358-0.581~\rm g/cm^3$, with some values exceeding $0.424~\rm g/cm^3$ (Tables 3 and 4). Zhou et al. (2018) have also reported the abnormally high values by this method and indicated that this is not the preferred method to determining $\rho_{\rm ad}$. In addition, Gensterblum et al. (2010) indicated that the $\rho_{\rm ad}$ obtained by this method could be overestimated. Results of fitted excess adsorption at 333.15 K using the slope densities are shown in Fig. 3c–d. It is clear that regardless of the excess adsorption models of Langmuir or *SDR*, there is a marked difference between the measured and fitted adsorption amount. It is, therefore, suggested that the slope density is not applicable for these two Yanchang mudstones.

As shown in Fig. 3 e-h, the fitted adsorption isotherms derived from different models with freely fitted ρ_{ad} generally show a good fit with the measured adsorption data at 333.15 K. The freely fitted ρ_{ad} of Langmuir and Langmuir-Henry models are 0.250–0.382 g/ cm³, and the fitting performance of the Langmuir-Henry model $(AIC_c ext{ of } -142.70 ext{ and } -147.04 ext{ for Samples Y-1 and Y-2, respectively})$ is better than that of the Langmuir model (AIC_c of -119.70and -112.07 for Samples Y-1 and Y-2, respectively) (Fig. 3e-f, Tables 3 and 4). The fitted ρ_{ad} based on the SDR and SDR-Henry models are 0.253-0.483 g/cm³, with some values in excess of 0.424 g/cm³ at 333.15 K and 363.15 K for Sample Y-1, which may indicate that a portion of methane is absorbed or dissolved in the residual organic matter in samples due to their relatively high S₁ values (Topór et al., 2017) (Table 1). Similarly, the fitting results based on the SDR-Henry model (AIC_c of -142.16 and -146.04 for Samples Y-1 and Y-2, respectively) show much a better correspondence with the measured excess adsorption amount than that based on the SDR model (AIC_c of -110.76 and -99.16 for Samples Y-1 and Y-2, respectively) (Fig. 3g-h, Tables 3 and 4).

Tables 3 and 4 contain the fitted parameters and AIC_c goodness-of-fit parameters based on different excess adsorption models with fixed, slope, and freely fitted densities for Samples Y-1 and Y-2. Overall, excess adsorption models with the fixed and slope densities have higher AIC_c values, which is consistent with the visual

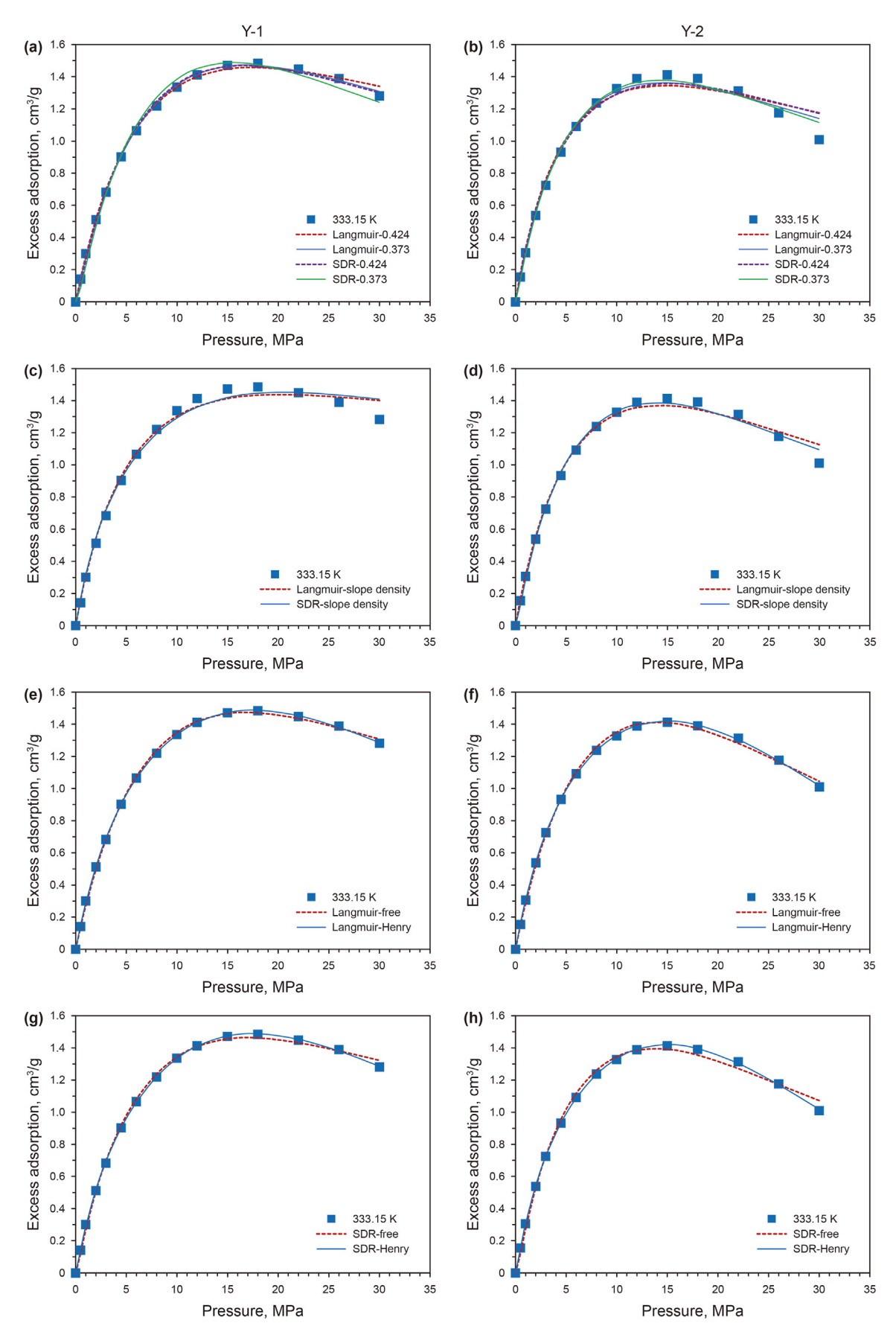


Fig. 3. Measured and fitted excess adsorption for samples at 333.15 K based on Langmuir and SDR models using various adsorbed-phase densities.

Table 3Fitted parameters based on different excess adsorption models of Sample Y-1.

Temperature	Excess models	n_0 , cm ³ /g	$P_{\rm L}$, MPa	$\rho_{\rm ad}$, g/cm ³	k	D	AIC_{c}
303.15 K	L-1	3.348	6.428	0.424		/	-102.67
	L-2	3.841	8.021	0.373	1	1	-112.80
	L-3	3.144	5.818	0.455	1	1	-94.08
	L-4	3.735	7.677	0.382	1	1	-110.55
	L-5	2.438	5.004	0.323	7.669	1	-138.36
	S-1	2.831	/	0.424	1	0.106	-115.59
	S-2	2.995	/	0.373	1	0.123	-90.07
	S-3	2.758	/	0.455	1	0.098	-101.59
	S-4	2.845	/	0.419	1	0.107	-112.99
	S-5	2.143	1	0.336	6.558	0.105	-134.43
333.15 K	L-1	3.101	9.759	0.424		/	-112.00
	L-2	3.548	11.833	0.373	1	1	-122.85
	L-3	2.746	8.150	0.496	1	1	-98.81
	L-4	3.571	11.943	0.371	1	1	-119.70
	L-5	1.860	6.722	0.306	8.988	1	-142.70
	S-1	2.483	/	0.424	1	0.124	-110.40
	S-2	2.597	/	0.373	1	0.142	-90.59
	S-3	2.381	/	0.496	1	0.107	-105.76
	S-4	2.443	/	0.448	1	0.117	-110.76
	S-5	1.424	1	0.309	9.533	0.114	-142.16
363.15 K	L-1	3.086	15.372	0.424		1	-111.23
	L-2	3.536	18.319	0.373	1	1	-120.20
	L-3	3.386	17.334	0.387	1	1	-117.43
	L-4	4.287	23.293	0.327	1	1	-124.01
	L-5	1.084	7.941	0.276	12.772	1	-139.46
	S-1	2.257	1	0.424	1	0.146	-104.80
	S-2	2.336	1	0.373	1	0.165	-92.70
	S-3	2.311	1	0.387	1	0.159	-96.35
	S-4	2.199	1	0.483	1	0.130	-107.45
	S-5	0.775	1	0.277	13.379	0.123	-143.87

L-1: Langmuir model fitted by the fixed density of $0.424 \, \text{g/cm}^3$; L-2: Langmuir model fitted by the fixed density of $0.373 \, \text{g/cm}^3$; L-3: Langmuir model fitted by slope density; L-4: freely fitted Langmuir model; L-5: freely fitted Langmuir-Henry model. S-1: *SDR* model fitted by the fixed density of $0.424 \, \text{g/cm}^3$; S-2: *SDR* model fitted by the fixed density of $0.373 \, \text{g/cm}^3$; S-3: *SDR* model fitted by slope density; S-4: freely fitted *SDR* model; S-5: freely fitted *SDR*-Henry model. n_0 is absolute adsorption capacity; P_L is the Langmuir pressure; ρ_{ad} is the adsorbed methane density; k is an empirical parameter in Henry equation; D is an interaction constant; AIC_c is the corrected Akaike's Information Criterion.

Table 4Fitted parameters based on different excess adsorption models of Sample Y-2.

Temperature	Excess models	n_0 , cm ³ /g	$P_{\rm L}$, MPa	$\rho_{\rm ad}$, g/cm ³	k	D	AICc
303.15 K	L-1	2.781	4.078	0.424		1	-86.42
	L-2	3.111	4.983	0.373	1	1	-106.16
	L-3	2.320	2.903	0.581	1	1	-66.27
	L-4	3.338	5.625	0.350	1	1	-111.72
	L-5	2.542	4.281	0.308	5.573	1	-126.75
	S-1	2.560	1	0.424	1	0.086	-84.85
	S-2	2.706	1	0.373	1	0.099	-119.45
	S-3	2.320	1	0.581	1	0.063	-59.38
	S-4	2.733	1	0.365	1	0.102	-120.27
	S-5	2.352	1	0.324	3.864	0.100	-129.53
333.15 K	L-1	2.490	6.397	0.424		1	-80.70
	L-2	2.776	7.586	0.373	1	1	-89.21
	L-3	2.894	8.090	0.358	1	1	-92.93
	L-4	3.801	12.075	0.295	1	1	-112.07
	L-5	1.776	5.982	0.261	10.230	1	-147.04
	S-1	2.204	1	0.424	1	0.104	-83.14
	S-2	2.307	1	0.373	1	0.118	-96.50
	S-3	2.346	1	0.358	1	0.124	-100.63
	S-4	2.386	1	0.344	1	0.130	-99.16
	S-5	1.358	1	0.263	10.750	0.117	-146.04
363.15 K	L-1	2.344	9.770	0.424	1	1	-98.42
	L-2	2.614	11.408	0.373	1	1	-105.38
	L-3	2.569	11.128	0.380	1	1	-104.25
	L-4	3.404	16.328	0.303	1	1	-113.13
	L-5	0.985	5.556	0.250	12.499	1	-133.02
	S-1	1.951	1	0.424	1	0.120	-103.72
	S-2	2.021	1	0.373	1	0.136	-105.09
	S-3	2.009	1	0.380	1	0.133	-105.76
	S-4	1.993	1	0.391	1	0.130	-102.96
	S-5	0.838	1	0.253	12.230	0.116	-133.97

evaluation of their poor fit (Fig. 3a–d), and excess adsorption models with the freely fitted density show relatively lower $AIC_{\rm C}$ values (Fig. 4). By contrast, the fitting results of Langmuir-Henry and SDR-Henry models exhibit the lowest $AIC_{\rm C}$ values, showing the minimum difference between the fitted and measured adsorption amounts. For comparison, Dang et al. (2020) compared the fitting performance of different models on Shanxi and Benxi Shales from Ordos Basin and demonstrated that the SDR-Henry is the best fitting one since it shows the least fitting error.

Consequently, if only the fitting performance and errors are considered, it is appearing that the Langmuir-Henry and *SDR*-Henry models using freely fitted adsorbed methane densities are the best methods available to correct and fit excess adsorption isotherms and obtain absolute adsorption amounts for samples in this study.

However, it should be noted that the model with the lowest fitting error may not be the best model, since it can have too many free fitting parameters, and so obtain higher fitting precision but lose its physical meaning (Tang et al., 2017). Consequently, the converted absolute adsorption isotherms should be further evaluated to determine the optimal models.

3.3.2. Absolute adsorption isotherms

Once ρ_{ad} was determined, the measured adsorption amount was corrected as the absolute adsorption amount [Eq. (2)]. Fig. 5 shows the absolute adsorption isotherms derived from different models (Langmuir, Langmuir-Henry, SDR, and SDR-Henry models) with the freely fitted adsorbed methane densities. For Sample Y-1, all isotherms derived from these four excess models monotonically increase with an increasing pressure up to 30 MPa at the different experimental temperatures, and exhibit the distinct temperaturedependent feature (Fig. 5a-d). However, for Sample Y-2, the isotherms for 303.15 and 333.15 K intersect in the results of the SDR-Henry model (Fig. 5h), while the isotherms at 303.15 K and 333.15 K derived from Langmuir and Langmuir-Henry models would also intersect if the experimental pressures were slightly higher (Fig. 5e-f). The intersection of adsorption isotherms contradicts the principle in adsorption theory that a high temperature always negatively affects adsorption amount (Tang et al., 2017). Only isotherms derived from the SDR model are temperature-dependent for both Y-1 and Y-2 (Fig. 5c, g), showing that the adsorption uptake increases with an increasing pressure while decreases with an increasing temperature.

By comprehensively considering the fitting performance of different adsorption models and their derived absolute adsorption, the *SDR* model with freely fitted adsorbed-phase density yielded the best fit to the measured adsorption data. Consequently, this model and parameters derived from it will be applied to interpret the adsorption behavior in the following section.

3.4. Adsorption capacity and volume of adsorbed phase (V_{ab})

Based on the freely fitted *SDR* model, the adsorption capacities are 2.845, 2.443, and 2.199 cm³/g for Sample Y-1, and are 2.733, 2.386, and 1.993 cm³/g for Sample Y-2, at temperatures of 303.15, 333.15, and 363.15 K, respectively (Tables 3 and 4). The adsorption capacity is negatively correlated with temperature (Fig. 6), showing a temperature-dependent behavior.

Once the adsorbed methane density and the absolute adsorption amount were determined, the volume of the adsorbed methane (V_{ab}) in a sample can be obtained based on Eq. (2). Fig. 7 shows the relation between V_{ab} based on the SDR excess model and pressure for Samples Y-1 and Y-2 as well as the micropore volumes (PV_{micro}) for the samples. For methane adsorption at 303.15 and 333.15 K, the $V_{\rm ab}$ up to 30 MPa is larger than the corresponding PV_{micro} for both samples. However, at 363.15 K, the V_{ab} up to 30 MPa is similar to or smaller than the corresponding PV_{micro}. Since methane molecules are preferentially adsorbed into micropores and then successively in mesopores and macropores (Zhou et al., 2018), the comparison between V_{ab} and PV_{micro} can reflect the supercritical methane adsorption mechanism to some extent. Specifically, at the pressure of 30 MPa, the adsorbed methane is mainly contained in micropores at a relatively high temperature (e.g., 363.15 K), and it filled not only in micropores but also in mesoand macro-pores under relatively low temperatures (e.g., 303.15 and 333.15 K).

Considering that the Chang 7 Member of Yanchang Formation is currently normally pressured (Liu et al., 2012, 2015), the approximate formation pressures of the two studied mudstones are 27 and 21 MPa, respectively [density of the formation water is 1.04 g/cm³ as reported by Tian et al. (2018)]. Additionally, the formation temperatures generally range from 70 to 100 °C (*i.e.*, 343.15–373.15 K) (Xu et al., 2019). Consequently, the adsorption analyses at 363.15 K approximately reflect the gas adsorption isotherms under the actual geological conditions. The $V_{\rm ab}$ value for this

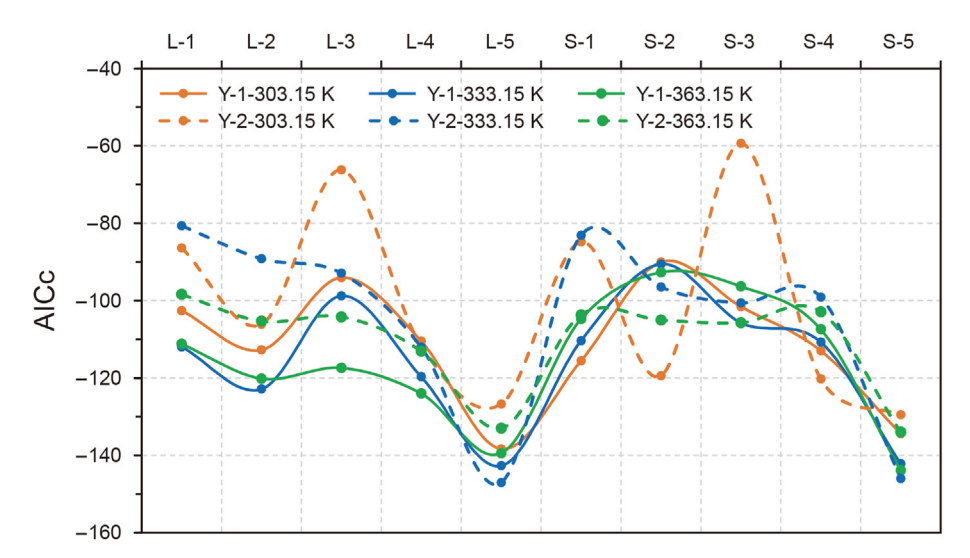


Fig. 4. Fitting error (AIC_c) between the measured and fitted adsorption amounts using different models adsorbed methane densities. The letter-number notations of x-axis represent the different excess adsorption models as shown in Table 3.

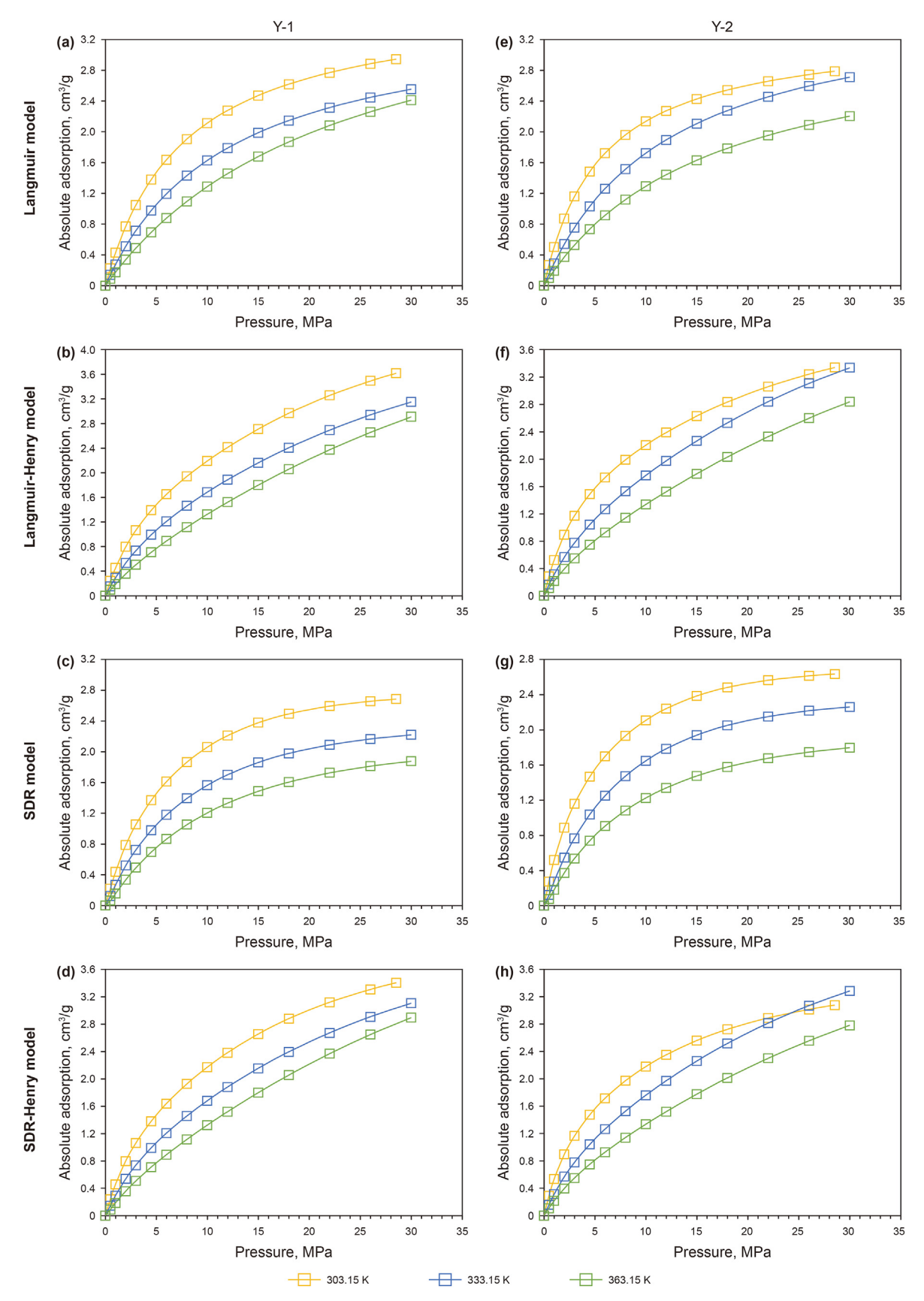


Fig. 5. Absolute adsorption isotherms of Samples Y-1 and Y-2 derived from different models with freely fitted adsorbed-phase density.

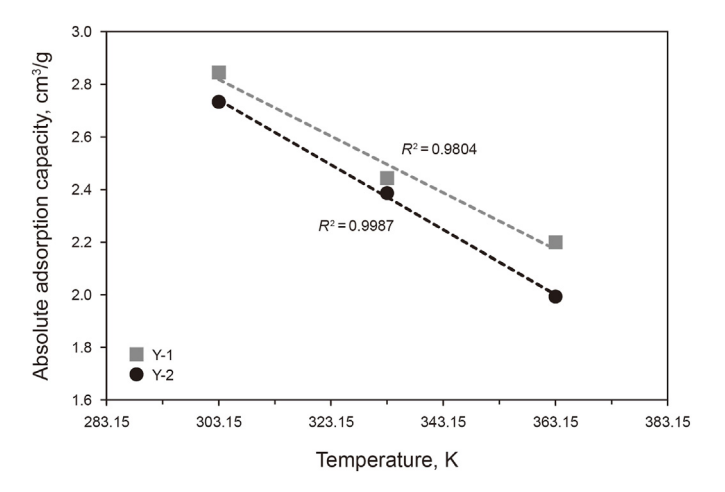


Fig. 6. Correlation of adsorption capacity derived from SDR model and temperature.

isotherm is close to the $PV_{\rm micro}$ in Sample Y-1, and is far less than the $PV_{\rm micro}$ in Sample Y-2 at the approximate formation pressures (Fig. 7). Meanwhile, considering that the gas generation potential in the Chang 7 mudstones is limited within the oil window ($R_{\rm o}$ 0.55%—0.66%), the adsorbed gas should be predominantly stored in micropores under actual geological conditions, which also confirms the rationale of choosing the SDR model based on the micropore-filling mechanism.

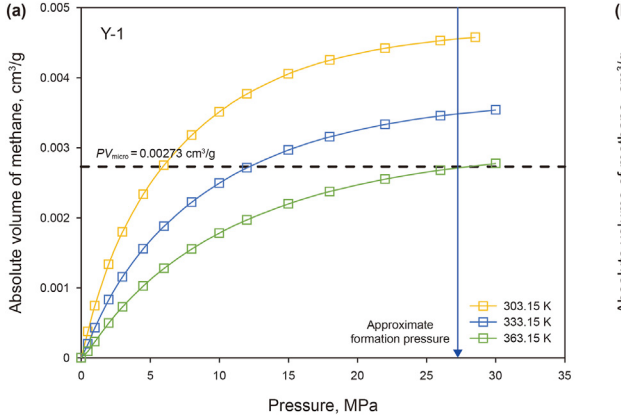
3.5. Thermodynamics of methane adsorption

3.5.1. Isosteric heat of adsorption at specific surface coverage (q_{st})

Generally, the $q_{\rm st}$ value varies with absolute adsorption amounts (Tian et al., 2016). Consequently, the $q_{\rm st}$ values were calculated at four different absolute adsorption amounts (*i.e.*, 0.4, 1.1, 1.5, and 1.8 cm³/g) for samples studied here. The pressures corresponding to these absolute adsorption amounts at different temperatures (303.15, 333.15, and 363.15 K) were calculated using the *SDR* excess adsorption model with freely fitted adsorbed-phase density. Fig. 8 shows the correlations between $\ln P$ and 1/T, and the $q_{\rm st}$ value at specific absolute adsorption amount can be obtained from the slope of the corresponding linear fitting line as shown in Eqs. (10) and (11).

The $q_{\rm st}$ values at different absolute adsorption amounts for Sample Y-1 range from 15.0 to 18.7 kJ/mol (avg. 16.3 kJ/mol) and that for Sample Y-2 range from 16.5 to 22.6 kJ/mol (avg. 18.5 kJ/mol) (Table 5). Both average $q_{\rm st}$ values are close to these calculated at the adsorption amount of 1.5 cm³/g (n_3). It is, therefore, indicated that the adsorption of supercritical methane onto the studied mudstones belongs to physisorption (generally with $q_{\rm st}$ < 40 kJ/mol), and the binding force between the methane molecule and rock surfaces belongs to van der Waals force (Zhou et al., 2019).

Generally, the $q_{\rm st}$ values remain relatively constant at the lower absolute adsorption amounts, but then begin to increase with increasing absolute adsorption amounts (Fig. 9). This observed behavior is different from both the monotonically increase of $q_{\rm st}$ with increasing adsorption amounts on the Shanxi and Benxi



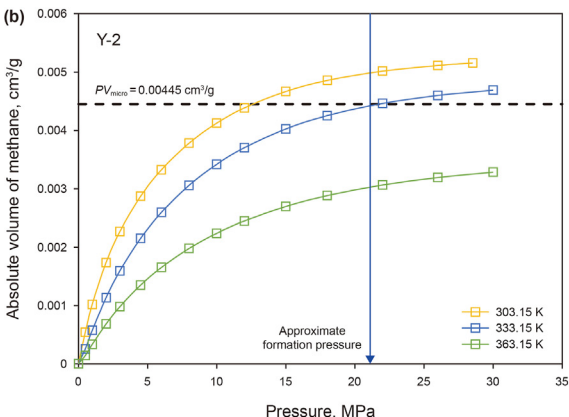
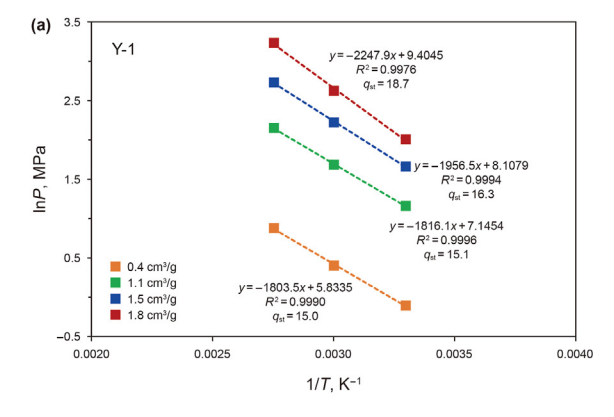


Fig. 7. The volume of adsorbed methane vs. pressure of Samples Y-1 and Y-2 derived from SDR excess adsorption models with freely fitted adsorbed-phase density. PV_{micro} is micropore volume.



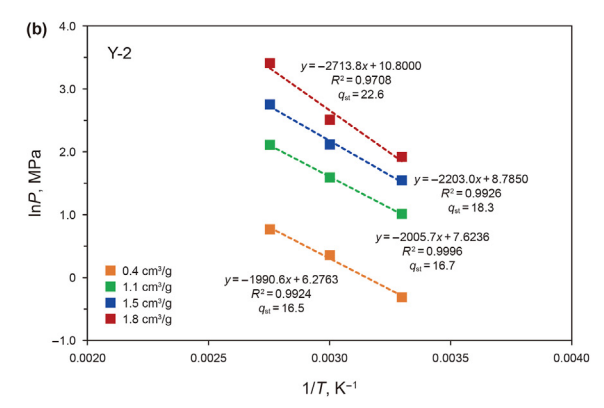
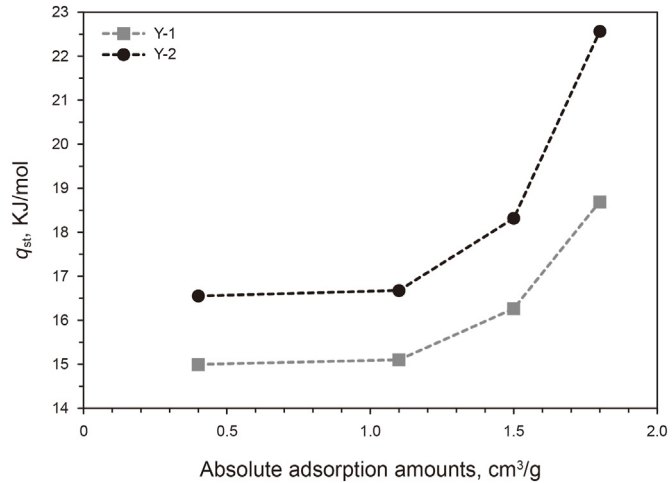


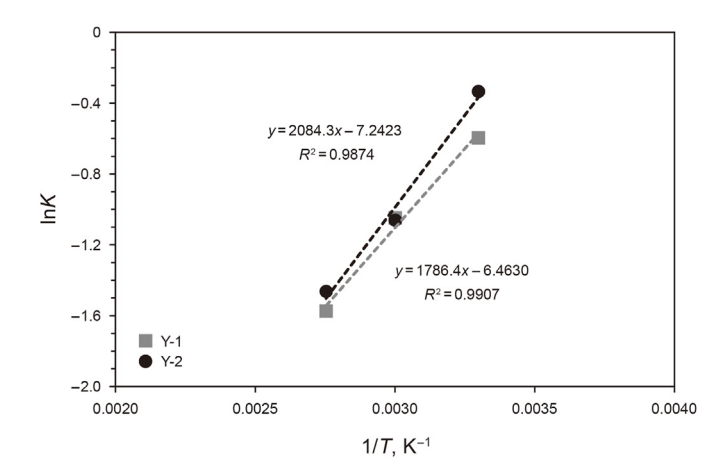
Fig. 8. Plot of ln*P* vs. 1/*T*.

 Table 5

 Thermodynamic parameters at different absolute adsorption amounts of methane (n).

Sample	n, cm ³ /g		Fitting of lnP vs. $1/T$		q _{st} , kJ/mol	ΔS ⁰ , J/mol/K	Average q _{st} , kJ/mol	Average ΔS^0 , J/mol/K	
			Slope	Intercept					
Y-1	n_1	0.4	-1803.5	5.8335	15.0	-67.6	16.3	-82.5	
	n_2	1.1	-1816.1	7.1454	15.1	-78.6			
	n_3	1.5	-1956.5	8.1079	16.3	-86.6			
	n_4	1.8	-2247.9	9.4045	18.7	-97.3			
Y-2	n_1	0.4	-1990.6	6.2763	16.5	-71.3	18.5	-88.7	
	n_2	1.1	-2005.7	7.6236	16.7	-82.5			
	n_3	1.5	-2203.0	8.7850	18.3	-92.2			
	n_4	1.8	-2713.8	10.800	22.6	-108.9			





Absolute adsorption amounts, cm³/g Fig. 11. Plot of lnK vs. 1/T.



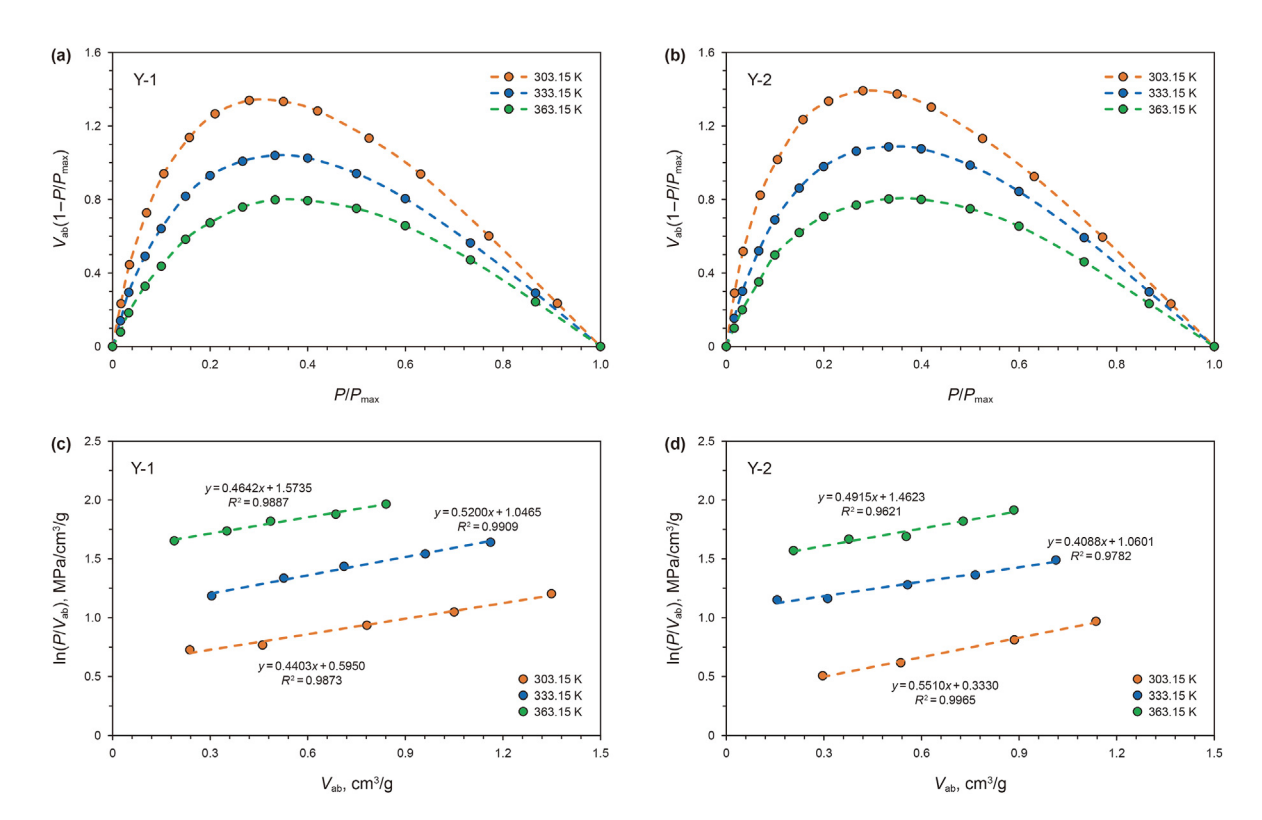


Fig. 10. Plot of $V_{ab} \cdot (1-P/P_{max})$ vs. P/P_{max} of (a) Sample Y-1 and (b) Sample Y-2; Plot of $\ln(P/V_{ab})$ vs. V_{ab} of (c) Sample Y-1 and (d) Sample Y-2.

Table 6 Fitting parameters for q_{st}^0 calculation.

Sample	Temperature, K	Fitting of ln(I	Fitting of $ln(P/V_{ab})$ vs. V_{ab}		Fitting of lnK	q _{st} , kJ/mol	
		Slope	Intercept		Slope	Intercept	
Y-1	303.15 333.15 363.15	0.4403 0.5200 0.4642	0.5950 1.0465 1.5735	-0.5950 -1.0465 -1.5735	1786.4	-6.4630	14.9
Y-2	303.15 333.15 363.15	0.5510 0.4088 0.4915	0.3330 1.0601 1.4623	-0.3330 -1.0601 -1.4623	2084.3	-7.2423	17.3

Shales from Ordos Basin reported by Dang et al. (2020), and the decreasing trend of q_{st} with increasing adsorption amount in Wufeng-Longmaxi Shales reported by Tian et al. (2016) and Zhou et al. (2019). Generally, q_{st} values at different absolute adsorption amounts are jointly controlled by the heterogeneity of the sample surface and the interaction forces between methane molecules (Yang et al., 2014). On the one hand, the heterogeneity of the sample surface would cause the q_{st} value to decrease with increasing absolute adsorption amount. Methane molecules preferentially occupy the adsorption sites with higher surface energy, followed by adsorption sites with relative lower surface energy, which causes the activation energy required for adsorption to increases, and consequently the $q_{\rm st}$ decreases. In addition, the interaction forces between methane molecules increase with increasing absolute adsorption amount, which contributes to the increased q_{st} values. Generally, the greater the adsorption amount, the greater the adsorption heat, and the more difficult it is for adsorption to occur. Therefore, whether the $q_{\rm st}$ increases or decreases with increasing absolute adsorption amount depends on which factors are dominant. For samples studied here, the unchanged q_{st} value at lower adsorption amount is likely affected by both the abovementioned two factors, while the increased q_{st} values at relative higher adsorption amount range are strongly controlled by the interaction energy between methane molecules.

The enthalpy change (ΔH) equals the negative of the $q_{\rm st}$ in value [e.g., Eq. (11)], which averages -16.3 kJ/mol for Sample Y-1 and -18.5 kJ/mol for Sample Y-2. The negative value of ΔH reveals that the methane-mudstone adsorption is an exothermic process. Based on Eq. (10), entropy change (ΔS^0) can be determined from the intercept of the fitting line between $\ln P$ vs. 1/T as shown in Fig. 8. The results show that ΔS^0 values for Sample Y-1 range from -97.3 to -67.6 J/mol/K (avg. -82.5 J/mol/K) and that for Sample Y-2 range from -108.9 to -71.3 J/mol/K (avg. -88.7 J/mol/K) (Table 5). The larger the $q_{\rm st}$ value and the lower the ΔS^0 value, the stronger the adsorption of methane molecule onto the sample surface. Consequently, the thermodynamic data suggest that the methane adsorption onto Sample Y-2 is relatively stronger than on Sample Y-1.

3.5.2. Isosteric heat of adsorption at zero surface coverage (q_{st}^0)

The main factors that affect the gas adsorption on a solid surface include specific surface area, adsorption amount per surface area, and interaction force between gas molecule and sample surface (Yang et al., 2014). Considering that the $q_{\rm st}$ value is related to the specific absolute adsorption amount, the $q_{\rm st}^0$ is an unbiased value of isosteric heat of adsorption, which is generally used to reflect the interaction force between methane molecule and rock surface. Fig. 10a—b displays the correlation between $V_{\rm ab} \cdot (1-P/P_{\rm max}) \ vs. \ P/P_{\rm max}$, which indicates the valid pressure range that complies with Henry's Law. Fig. 10c—d shows the correlation between $\ln(P/V_{\rm ab}) \ vs. \ V_{\rm ab}$ within the valid pressure range to calculate the a_0 and further determine the $\ln K$ value. Fig. 11 shows the plot of $\ln K \ vs. \ 1/T \ to determine the <math>q_{\rm st}^0$ based on Eq. (13). The results show that the $q_{\rm st}^1$ is 14.9 k|/mol for Sample Y-1 and 17.3 k|/mol for Sample Y-2 (Table 6).

The $q_{\rm st}^0$ is lower than the average $q_{\rm st}$ value for both Samples Y-1 and Y-2. It is consistent with the phenomenon that the $q_{\rm st}$ initially decreases and then remains unchanged with decreasing absolute adsorption amount (Fig. 9). Consequently, as the pressure is lowered to 0 (i.e., $V_{\rm ab} \rightarrow 0$), the $q_{\rm st}$ gradually decreases and finally remains unchanged. Although the absolute adsorption capacity of Sample Y-1 is higher than that of Sample Y-2 (Fig. 6), the interaction force between methane molecule and surface of Sample Y-2, as reflected by the $q_{\rm st}^0$ values, is stronger than that of Sample Y-1. Similar phenomenon was also proposed by Yang et al. (2014) on Niutitang Shales in Sichuan Basin. This also confirms that the gasmudstone adsorption is a complex process which is not only affected by the interaction force between gas molecule and sample surface.

4. Conclusions

In this study, supercritical methane adsorption tests with the pressures of up to 30 MPa was performed on two Chang 7 mudstones at temperatures of 303.15, 333.15, and 363.15 K. The capabilities of different excess adsorption models (Langmuir, *SDR*, Langmuir-Henry, and *SDR*-Henry models) to predict the experimental methane adsorption isotherms were evaluated using various adsorbed-phase densities (fixed, slope, and freely fitted densities), and the thermodynamics of methane-mudstone adsorption were determined. Regarding the two mudstones studied here, four main conclusions can be reached:

- (1) The SDR model with freely fitted adsorbed-phase density is the more reliable model to obtain the density of adsorbedphase methane, to interpret supercritical methanemudstone adsorption behaviors, and to determine absolute adsorption isotherms.
- (2) Gas adsorption capacity derived from the *SDR* adsorption model is temperature-dependent.
- (3) Methane molecules in the adsorbed phase predominantly occupy micropore (d < 2 nm) volume in the Chang 7 mudstone under the actual geological conditions.
- (4) Methane-mudstone adsorption is jointly controlled by the heterogeneity of, and interaction forces between methane molecules and, rock surfaces.

Acknowledgments

This work was supported by the Natural Science Basic Research Program of Shaanxi [No. 2022JQ-291; 2021JQ-234], the China Postdoctoral Science Foundation [No. 2021M692735], and the Fundamental Research Funds for the Central Universities, Chang'an University [No. 300102271305].

References

Chen, L., Liu, K.Y., Jiang, S., et al., 2020. Effect of adsorbed phase density on the

correction of methane excess adsorption to absolute adsorption in shale. Chem. Eng. J. 420, 127678. https://doi.org/10.1016/j.cej.2020.127678.

- Curtis, J.B., 2002. Fractured shale-gas systems. Am. Assoc. Petrol. Geol. Bull. 86 (11), 1921–1938. https://doi.org/10.1306/61EEDDBE-173E-11D7-8645000102C1865D.
- Dang, W., Zhang, J.C., Nie, H.K., et al., 2020. Isotherms, thermodynamics and kinetics of methane-shale adsorption pair under supercritical condition: implications for understanding the nature of shale gas adsorption process. Chem. Eng. J. 383, 123191. https://doi.org/10.1016/j.cej.2019.123191.
- Gao, Z.Y., Fan, Y.P., Hu, Q.H., et al., 2020. The effects of pore structure on wettability and methane adsorption capability of Longmaxi Formation shale from the southern Sichuan Basin in China. Am. Assoc. Petrol. Geol. Bull. 104 (6), 1375–1399. https://doi.org/10.1306/01222019079.
- Gasparik, M., Bertier, P., Gensterblum, Y., et al., 2014. Geological controls on the methane storage capacity in organic-rich shales. Int. J. Coal Geol. 123, 34–51. https://doi.org/10.1016/i.coal.2013.06.010.
- Gensterblum, Y., Hemert, P.V., Billemont, P., et al., 2010. European inter-laboratory comparison of high pressure CO₂ sorption isotherms II: Natural coals. Int. J. Coal Geol. 84 (2), 115–124. https://doi.org/10.1016/j.coal.2010.08.013.

 Gensterblum, Y., Merkel, A., Busch, A., et al., 2013. High-pressure CH₄ and CO₂
- Gensterblum, Y., Merkel, A., Busch, A., et al., 2013. High-pressure CH₄ and CO₂ sorption isotherms as a function of coal maturity and the influence of moisture. Int. J. Coal Geol. 118, 45–57. https://doi.org/10.1016/j.coal.2013.07.024.
- Guan, M., Liu, X.P., Jin, Z.J., et al., 2020. The heterogeneity of pore structure in lacustrine shales: insights from multifractal analysis using N₂ adsorption and mercury intrusion. Mar. Petrol. Geol. 114, 104150. https://doi.org/10.1016/j.marpetgeo.2019.104150.
- Guo, R.L., Zhao, Y.D., Wang, W.B., et al., 2020. Application of rare-earth elements and comparison to molecular markers in oil-source correlation of tight oil: a case study of Chang 7 of the Upper Triassic Yanchang Formation in Longdong area, Ordos Basin, China. ACS Omega 5 (35), 22140–22156. https://doi.org/10.1021/ acsomega.0c02233.
- Guo, W., Xiong, W., Gao, S.S., et al., 2013. Impact of temperature on the isothermal adsorption/desorption of shale gas. Petrol. Explor. Dev. 40 (4), 514–519. https://doi.org/10.1016/S1876-3804(13)60066-X.
- Han, S.J., Sang, S.X., Duan, P.P., et al., 2022a. The effect of the density difference between supercritical CO₂ and supercritical CH₄ on their adsorption capacities: an experimental study on anthracite in the Qinshui Basin. Petrol. Sci. https://doi.org/10.1016/j.petsci.2022.03.003. Online published.
- Han, M.L., Wei, X.L., Zhang, J.C., et al., 2022b. Influence of structural damage on evaluation of microscopic pore structure in marine continental transitional shale of the Southern North China Basin: a method based on the low-temperature N₂ adsorption experiment. Petrol. Sci 19, 100–115. https://doi.org/10.1016/j.petsci.2021.10.016.
- Hou, Y.G., He, S., Yi, J.Z., et al., 2014. Effect of pore structure on methane sorption potential of shales. Petrol. Explor. Dev. 41 (2), 272–281. https://doi.org/10.1016/ \$1876-3804(14)60033-1.
- Huang, H.X., Li, R.X., Xiong, F.Y., et al., 2020a. A method to probe the pore-throat structure of tight reservoirs based on low-field NMR: insights from a cylindrical pore model. Mar. Petrol. Geol. 117, 104344. https://doi.org/10.1016/ i.marnetgeo.2020.104344.
- Huang, H.X., Li, R.X., Jiang, Z.X., et al., 2020b. Investigation of variation in shale gas adsorption capacity with burial depth: insights from the adsorption potential theory. J. Nat. Gas Sci. Eng. 73, 103043. https://doi.org/10.1016/ j.jngse.2019.103043.
- Huang, H.X., Li, R.X., Chen, W.T., et al., 2021. Revisiting movable fluid space in tight fine-grained reservoirs: a case study from Shahejie shale in the Bohai Bay Basin, NE China. J. Petrol. Sci. Eng. 207, 109170. https://doi.org/10.1016/ j.petrol.2021.109170.
- Kim, C., Devegowda, D., 2022. Molecular dynamics study of fluid-fluid and solid-fluid interactions in mixed-wet shale pores. Fuel 319, 123587. https://doi.org/10.1016/j.fuel.2022.123587.
- Kuang, L.C., Hou, L.H., Wu, S.T., et al., 2022. Organic matter occurrence and poreforming mechanisms in lacustrine shales in China. Petrol. Sci. https://doi.org/ 10.1016/j.petsci.2022.03.005. Online published.
- Li, J., Chen, Z.X., Wu, K.L., et al., 2018b. A multi-site model to determine supercritical methane adsorption in energetically heterogeneous shales. Chem. Eng. J. 349, 438–455. https://doi.org/10.1016/j.cej.2018.05.105.
- Li, J., Zhou, S.X., Gaus, G., et al., 2018a. Characterization of methane adsorption on shale and isolated kerogen from the Sichuan Basin under pressure up to 60 MPa: experimental results and geological implications. Int. J. Coal Geol. 189, 83–93. https://doi.org/10.1016/j.coal.2018.02.020.
- Li, T.F., Tian, H., Xiao, X.M., et al., 2017. Geochemical characterization and methane adsorption capacity of overmature organic-rich Lower Cambrian shales in northeast Guizhou region, southwest China. Mar. Petrol. Geol. 86, 858–873. https://doi.org/10.1016/j.marpetgeo.2017.06.043.
- Liu, J.J., Liu, Z., Zhu, W.Q., et al., 2015. Characteristics of mudstone compaction and paleo-pressure restoration of Chang 7 shale in the middle of Shanbei Slope. Geosci. 29 (3), 633–643 (in Chinese).
- Liu, K.Q., Jin, Z.J., Zeng, L.B., et al., 2022a. Microstructural analysis of organic matter in shale by SAXS and WAXS methods. Petrol. Sci. https://doi.org/10.1016/ i.petsci.2022.01.012.
- Liu, P., Wang, X.F., Li, X.F., et al., 2020b. Competitive adsorption characteristics of CH₄/C₂H₆ gas mixtures on model substances, coal and shale. Fuel 279, 118038. https://doi.org/10.1016/j.fuel.2020.118038.
- Liu, P., Wang, X.F., Lin, Y., et al., 2020a. Chemical and carbon isotope fractionations of

- alkane gases desorbed from confined systems and the application toward shale gas reservoir. Mar. Petrol. Geol. 113, 104103. https://doi.org/10.1016/j.marpetgeo.2019.104103.
- Liu, X.P., Guan, M., Jin, Z.J., et al., 2022b. Pore structure evolution of lacustrine organic-rich shale from the second member of the Kongdian formation in the Cangdong Sag, Bohai Bay Basin, China. Petrol. Sci 19, 459–471. https://doi.org/ 10.1016/j.petsci.2021.12.010.
- Liu, Z., Chen, K., Zhu, W.Q., et al., 2012. Paleo-pressure restoration of Chang 7 shale in Xifeng area, Ordos Basin. J. China Univ. Pet. 36 (2), 1–7 (in Chinese).
 Liu, Z.H., Wang, J.C., Bai, B.J., et al., 2022c. Impact of clay stabilizer on the methane
- Liu, Z.H., Wang, J.C., Bai, B.J., et al., 2022c. Impact of clay stabilizer on the methane desorption kinetics and isotherms of Longmaxi Shale. China. Petrol. Sci 19 (1), 234–244. https://doi.org/10.1016/j.petsci.2021.09.025.
- Luo, Q.Y., Fariborz, G., Zhong, N.N., et al., 2020. Graptolites as fossil geothermometers and source material of hydrocarbons: an overview of four decades of progress. Earth Sci. Rev. 200, 103000. https://doi.org/10.1016/j.earscirev.2019.103000.
- Luo, Q.Y., George, S.C., Xu, Y.H., et al., 2016a. Organic geochemical characteristics of the Mesoproterozoic Hongshuizhuang Formation from northern China: implications for thermal maturity and biological sources. Org. Geochem. 99, 23–37. https://doi.org/10.1016/j.orggeochem.2016.05.004.
- Luo, Q.Y., Hao, J.Y., Skovsted, C.B., et al., 2018. Optical characteristics of graptolite-bearing sediments and its implication for thermal maturity assessment. Int. J. Coal Geol. 195, 386–401. https://doi.org/10.1016/j.coal.2018.06.019.
- Luo, Q.Y., Zhang, L., Zhong, N.N., et al., 2021. Thermal evolution behavior of the organic matter and a ray of light on the origin of vitrinite-like maceral in the Mesoproterozoic and Lower Cambrian black shales: insights from artificial maturation. Int. J. Coal Geol. 244, 103813. https://doi.org/10.1016/i.coal.2021.103813.
- Luo, Q.Y., Zhong, N.N., Dai, N., et al., 2016b. Graptolite-derived organic matter in the Wufeng—Longmaxi formations (Upper Ordovician—lower Silurian) of southeastern Chongqing, China: implications for gas shale evaluation. Int. J. Coal Geol. 153, 87—98. https://doi.org/10.1016/j.coal.2015.11.014.
- Onawole, A.T., Nasser, M.S., Hussein, I.A., et al., 2021. Theoretical studies of methane adsorption on silica-kaolinite interface for shale reservoir application. Appl. Surf. Sci. 546, 149164. https://doi.org/10.1016/j.apsusc.2021.149164.
- Psarras, P., Holmes, R., Vishal, V., et al., 2017. Methane and CO₂ adsorption capacities of kerogen in the Eagle Ford shale from molecular simulation. Acc. Chem. Res. 50 (8), 1818–1828. https://doi.org/10.1021/acs.accounts.7b00003.
- Rani, S., Padmanabhan, E., Prusty, B.K., 2019. Review of gas adsorption in shales for enhanced methane recovery and CO₂ storage. J. Pet. Sci. Eng. 175, 634–643. https://doi.org/10.1016/j.petrol.2018.12.081.
- Rexer, T.F.T., Benham, M.J., Aplin, A.C., et al., 2013. Methane adsorption on shale under simulated geological temperature and pressure conditions. Energy Fuels 27 (6), 3099–3109. https://doi.org/10.1021/ef400381v.
- Song, X., Lu, X.X., Shen, Y.Q., et al., 2018. A modified supercritical Dubinin-Radushkevich model for the accurate estimation of high pressure methane adsorption on shales. Int. J. Coal Geol. 193, 1–15. https://doi.org/10.1016/j.coal.2018.04.008.
- Strapoć, D., Mastalerz, M., Schimmelmann, A., et al., 2010. Geochemical constraints on the origin and volume of gas in the new Albany Shale (Devonian-Mississippian), eastern Illinois Basin. Am. Assoc. Petrol. Geol. Bull. 94 (11), 1713–1740. https://doi.org/10.1306/06301009197.
- Sugiura, N., 1978. Further analysis of the data by Akaike's information criterion and the finite corrections. Commun. Stat-Theor. M. A7 (1), 13–26. https://doi.org/ 10.1080/03610927808827599.
- Tang, X., Ripepi, N., Luxbacher, K., et al., 2017. Adsorption models for methane in shales: review, comparison, and application. Energy Fuels 31 (10), 10787–10801. https://doi.org/10.1021/acs.energyfuels.7b01948.
- Thommes, M., Kaneko, K., Neimark, A.V., et al., 2015. Physisorption of gases, with special reference to the evaluation of surface area and pore size distribution (IUPAC Technical Report). Pure Appl. Chem. 87 (9–10), 1051–1069. https://doi.org/10.1515/pac-2014-1117.
- Tian, H., Li, T.F., Zhang, T.W., et al., 2016. Characterization of methane adsorption on overmature Lower Silurian-Upper Ordovician shales in Sichuan Basin, southwest China: experimental results and geological implications. Int. J. Coal Geol. 156, 36–49. https://doi.org/10.1016/j.coal.2016.01.013.
- Tian, J., Kang, Y.L., Luo, P.Y., et al., 2018. Experimental simulation of initial water saturation forming process in tight reservoirs: a case study of Chang 7 tight oil reservoir in Ordos Basin, NW China. Xinjing Pet. Geol. 39 (6), 701–707 (in Chingso)
- Topór, T., Derkowski, A., Ziemiański, P., et al., 2017. Multi-variable constraints of gas exploration potential in the Lower Silurian shale of the Baltic Basin (Poland). Int. J. Coal Geol. 179, 45–59. https://doi.org/10.1016/j.coal.2017.05.001.
- Wang, T.Y., Tian, S.C., Liu, Q.L., et al., 2021a. Pore structure characterization and its effect on methane adsorption in shale kerogen. Petrol. Sci. 18, 565–578. https:// doi.org/10.1007/s12182-020-00528-9.
- Wang, Y., Cheng, H.F., Hu, Q.H., et al., 2022. Pore structure heterogeneity of Wufeng-Longmaxi shale, Sichuan Basin, China: evidence from gas physisorption and multifractal geometries. J. Pet. Sci. Eng. 208, 109313. https://doi.org/10.1016/ i.petrol.2021.109313.
- Wang, Y., Liu, L.F., Cheng, H.F., et al., 2020a. Pore structure of Triassic Yanchang mudstone, Ordos Basin: insights into the impact of solvent extraction on porosity in lacustrine mudstone within the oil window. J. Pet. Sci. Eng. 195. https://doi.org/10.1016/j.petrol.2020.107944, 107944.
- Wang, Y., Liu, L.F., Cheng, H.F., 2021b. Gas adsorption characterization of pore

structure of organic-rich shale: insights into contribution of organic matter to shale pore network. Nat. Resour. Res. 30 (3), 2377–2395. https://doi.org/10.1007/s11053-021-09817-5.

- Wang, Y., Liu, L.F., Hu, Q.H., et al., 2020b. Nanoscale pore network evolution of Xiamaling marine shale during organic matter maturation by hydrous pyrolysis. Energy Fuels 34, 1548–1563. https://doi.org/10.1021/acs.energyfuels.9b03686.
- Wang, Y., Liu, L.F., Li, S.T., et al., 2017. The forming mechanism and process of tight oil sand reservoirs: a case study of Chang 8 oil layers of the Upper Triassic Yanchang Formation in the western Jiyuan area of the Ordos Basin, China. J. Pet. Sci. Eng. 158, 29—46. https://doi.org/10.1016/j.petrol.2017.08.026.
- Wang, Y., Liu, L.F., Sheng, Y., et al., 2019a. Investigation of supercritical methane adsorption of overmature shale in Wufeng-Longmaxi formation, Southern Sichuan Basin, China. Energy Fuels 33 (3), 2078–2089. https://doi.org/10.1021/acs.energyfuels.8b04344.
- Wang, Y., Liu, L.F., Zheng, S.S., et al., 2019b. Full-scale pore structure and its controlling factors of the Wufeng-Longmaxi shale, southern Sichuan Basin, China: implications for pore evolution of highly overmature marine shale. J. Nat. Gas Sci. Eng. 67, 134—146. https://doi.org/10.1016/j.jngse.2019.04.020.
 Weishauptová, Z., Přibyl, O., Sýkorová, I., et al., 2017. Effect of the properties of
- Weishauptová, Z., Přibyl, O., Sýkorová, I., et al., 2017. Effect of the properties of Silurian shales from the Barrandian Basin on their methane sorption potential.

- Fuel 203, 68-81. https://doi.org/10.1016/j.fuel.2017.04.087.
- Xu, Z.J., Liu, L.F., Liu, B.J.M., et al., 2019. Geochemical characteristics of the Triassic Chang 7 lacustrine source rocks, Ordos Basin, China: implications for paleoenvironment, petroleum potential and tight oil occurrence. J. Asian Earth Sci. 178, 112–138. https://doi.org/10.1016/j.jseaes.2018.03.005.
- Yang, F., Ning, Z.F., Wang, Q., et al., 2014. Thermodynamic analysis of methane adsorption on gas shale. J. Cent. South Univ. 45 (8), 2871–2877 (in Chinese).
- Yang, Y., Liu, S.M., 2020. Review of shale gas sorption and its models. Energy Fuels 34 (12), 15502–15524. https://doi.org/10.1021/acs.energyfuels.0c02906. Zhao, X.Z., Yang, Y.H., Sun, F.J., et al., 2016. Enrichment mechanism and exploration
- Zhao, X.Z., Yang, Y.H., Sun, F.J., et al., 2016. Enrichment mechanism and exploration and development technologies of high coal rank coalbed methane in south Qinshui Basin, Shanxi Province. Petrol. Explor. Dev. 43 (2), 332–339. https:// doi.org/10.1016/S1876-3804(16)30039-8.
- Zhou, S.W., Wang, H.Y., Zhang, P.Y., et al., 2019. Investigation of the isosteric heat of adsorption for supercritical methane on shale under high pressure. Adsorpt. Sci. Technol. 37, 590–606. https://doi.org/10.1177/0263617419866986.
- Technol. 37, 590–606. https://doi.org/10.1177/0263617419866986.

 Zhou, S.W., Xue, H.Q., Ning, Y., et al., 2018. Experimental study of supercritical methane adsorption in Longmaxi shale: insights into the density of adsorbed methane. Fuel 211, 140–148. https://doi.org/10.1016/j.fuel.2017.09.065.